# Detection and Segmentation of Various Types of Fluids with Graph Shortest Path and Deep Learning Approaches

Abdolreza Rashno*, Dara D. Koozekanani**, and Keshab K. Parhi*

*Department of Electrical and Computer Engineering,
University of Minnesota, Minneapolis, MN 55455, USA
**Department of Ophthalmology and Visual Neurosciences,
University of Minnesota, Minneapolis, MN 55455 USA,
{arashno,dkoozeka,parhi}@umn.edu

**Abstract.** Today, diagnosis and monitoring of retina diseases related to pathologies such as accumulated fluid can be performed using optical coherence tomography (OCT). OCT acquires a series of 2D slices (Bscans). This work presents a fully-automated method to segment and detect three types of fluid including sub-retinal fluid (SRF), intra-retinal fluid (IRF) and pigment epithelium detachment (PED) in OCT Bscans of subjects with age-related macular degeneration (AMD) and retinal vein occlusion (RVO) or diabetic retinopathy. Segmentation method is based on graph shortest path algorithms and convolutional neural network (CNN). Proposed method achieves an average dice coefficient of 76.44%, 92.25% and 82.14% in Cirrus, Spectralis and Topcon datasets, respectively.

**Keywords:** Optical Coherence Tomography; sub-retinal fluid; intra-retinal fluid; pigment epithelium detachment, graph shortest path; convolutional neural network.

## 1 Introduction

Optical coherence tomography (OCT) is a non-invasive and non-contact imaging method with extensive clinical use in ophthalmology. It uses optical technology to create tomographic images with variable scan rates and resolutions, and is used to create cross-sectional images of ocular tissues, including the retina [1]. It is extensively used clinically for the diagnosis and follow-up of patients with retinal vein occlusion (RVO) and age-related macular degeneration (AMD) [2].

The macula is the central part of the retina and is critical for good vision. RVO, manifested by fluid cysts within the retina and retinal thickening, is caused by fluid leakage from damaged macular blood vessels. This causes vision loss and is the most common cause of vision loss among working-aged adults in the United States. OCT images allow very sensitive detection and quantitative assessment of these fluid cysts and retinal thickening [3, 5, 7]. AMD is characterized by the

growth of abnormal blood vessels from the choroidal vasculature, and the resultant fluid leakage into the intra-retinal, sub-retinal, and sub-retinal pigment epithelium (RPE) spaces. The standard treatment for this condition is guided by the presence and quantity of this fluid [4, 6]. The fluid quantity cannot be routinely measured in clinical practice because commercial algorithms do not directly detect fluid. Some state of the art methods for fluid segmentation in AMD and RVO subjects were proposed in [2, 10, 8, 9, 12, 11].

In this work, a fully-automated method is presented for the segmentation of three types of fluid including intra-retinal fluid (IRF), sub-retinal fluid (SRF) and pigment epithelial detachment (PED). In the first step, inner limiting membrane (ILM) and retinal pigment epithelium (RPE) layers are segmented by graph shortest path methods. Then, the regions between these layers are input to a convolutional neural network (CNN). The CNN is trained for binary classification of pixels between ILM and RPE. In this application, both IRF and SRF fluids are considered as object and tissue is considered as background. Finally, PED is segmented by the proposed method based on layer segmentation and layer flattening.

The rest of this paper is organized as follows. Section 2 presents the proposed methodology with subsections including layer segmentation, PED segmentation with layer flattening, IRF and SRF segmentation with CNN, and fluid detection. Experimental results are presented in Section 3. Segmentation results are presented in Sections 4. Finally, conclusion is described in Sections 5.

## 2 Methods

The main contribution of this work is to segment and detect IRF, SRF and PED. IRF and SRF are located between ILM and RPE layers while PED is underneath RPE. The important property of IRF and SRF is that these fluid types stem from abnormal blood vessels leakage from the choroidal vasculature, and the resultant dark region. In PED fluid may or may not exist. In patients with early AMD, PED is the result of RPE elevation and fluid does not exist while in severe AMD RPE is elevated by fluid regions. The proposed approaches for fluid segmentation are in agreement with the mentioned properties of fluid regions. For IRF and SRF, a supervised method based on CNN is trained. PED is computed by the flattening of RPE which means that the elevated RPE is flattened and then the elevation of RPE is computed. It is not affected by the texture of PED. Therefore, both non-fluid PED and fluid PED can be segmented by this method.

### 2.1 Layer Segmentation

The first step of the proposed method is the segmentation of ILM and RPE layers as a ROI for IRF and SRF regions. This step is very important due to two aspects. First, the background region is very similar to fluid/cyst regions in both brightness and texture. This can easily *mislead* the CNN segmentation

method since this method is based on brightness of neighboring pixels of target pixel. The second reason for ROI segmentation is speeding up since the ROI is processed instead of the whole image. Therefore, ROI is presented in the train and test phases of CNN. For layer segmentation, the graph is constructed from each OCT Bscan by mapping each pixel in the image to one node in a graph. We only consider the local relationship between pixels. Therefore, by considering the local relationship for 8 neighbors of each pixel, the 8-regular graph is constructed. For ILM segmentation, the image is first filtered with a vertical gradient filter and then the weight computation between any two arbitrary pixels $(a_1, b_1)$ and $(a_2, b_2)$ is defined by (1):

$$\begin{aligned} W((a_1, b_1), (a_2, b_2)) = 4 * MaxG - VerGrad(a_1, b_1) \\ - VerGrad(a_2, b_2) + 2 * mean(R) \end{aligned} \tag{1}$$

where $MaxG$ is the maximum gray level of the image and $R$ is a set of $R$ pixels above $(a_1, b_1)$. In this work, $R$ is set to 10 based on experiments. The procedure for the segmentation of RPE is that the vertical gradient is inversed and $R$ corresponds to a set of $D$ pixels under $(a1, b1)$. Weight computation between any two arbitrary pixels is defined by (2):

$$W((a_1, b_1), (a_2, b_2)) = 4 * MaxG - VerGrad(a_1, b_1) - VerGrad(a_2, b_2) - mean(R) \tag{2}$$

### 2.2 PED segmentation with Layer flattening

As it was mentioned before, PED can not be segmented based on pixel intensities since in early AMD there is no fluid in PED while in severe AMD fluid exists. The proposed method for PED segmentation is to flatten the elevated RPE and compute the region between flattened RPE and elevated RPE. Segmented RPE in the previous section is the elevated RPE. To flatten RPE, first all pixels in RPE are considered as a vector in which $RPE(i)$ is the height of $ith$ pixel in RPE. When the RPE is elevated, a pick (or picks) are created. This pick is determined as a point with the maximum curvature. Then, the left and right sides where the curve begins and ends are found. Finally, left and right sides are connected by 1D linear interpolation which leads to the flattened RPE. Two samples of the flattened RPE results are shown in Fig. 1.

### 2.3 IRF and SRF segmentation with CNN

IRF and SRF fluid types are located between ILM and elevated RPE. Here, IRF and SRF segmentation are modeled as a supervised classification task in which fluid (IRF and SRF) and tissue pixels are labeled as 1 and 0, respectively. Therefore, CNN is trained for binary classification. It may be noted that in this step, both fluid types are classified as fluid. The type of fluid is determined based on Algorithm 1.

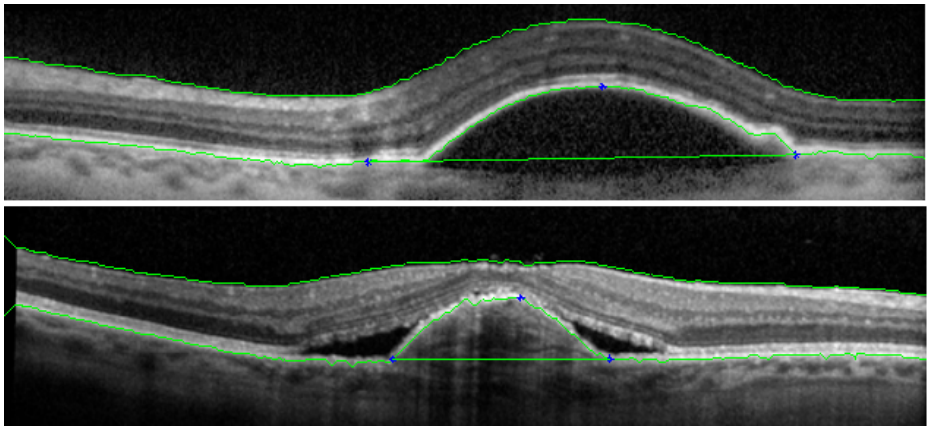

**Fig. 1.** Two samples of ILM and RPE segmentation results.

**Algorithm 1** IRF and SRF Labeling.

Inputs: Binary segmented image by CNN: SegBscan (fluid=1, tissue=0), Trshld=40.
Output:Labeled fluid pixels as IRF or SRF.
Find all connected components in SegBscan and save them in $CCom$.
**for** i=1:length($CCom$) **do**
    $CC = CCom(i)$
    **for** $j = 1$: length(CC) **do** ▷ All pixels in CC
        Find the vertical distance of pixel $j$ from the segmented elevated RPE (without flattening) and save it in $dist(j)$
    $MinDist = min(dist)$
    **if** $MinDist < Trshld$ **then**
        Label all pixels in CC as $SRF$.
    **else** Label all pixels in CC as $IRF$.
End.

### 2.4 Fluid Detection

Another contribution of this paper is fluid detection. For each Bscan, probabilities of the existence of IRF, SRF and PED are computed. In the next step, these probabilities are computed for each OCT volume. In this work, the probability of IRF, SRF and PED are computed by thresholding. Therefore, a binary value is assigned for each Bscan which means that this Bscan may or may not contain fluid. For each fluid type in a Bscan, $TrIRF = 110$, $RtSRF = 180$ and $TrPED = 85$ are considered as thresholds for IRF, SRF and PED detection, respectively. If the number of segmented pixels for each fluid type is bigger than corresponding threshold this probability is 1, otherwise it is 0.

## 3 Experimental results

To evaluate the proposed algorithms, released training data are divided into 2 groups, training and validation sets. Note that segmentation results for test set in challenge competition will be submitted after the submission of this paper. Train set contains 24 volumes from three manufacturers. For each manufacturer, 16 volumes are considered as training set and 8 volumes as validation set. PED segmentation is performed by the proposed layer segmentation and layer flattening methods. Therefore, it does not need a training set and can be applied in each OCT scan in an unsupervised manner. For IRF and SRF segmentation, three CNNs are constructed and trained for the OCT Bscans of each manufacturer. In each CNN, 16 OCT volumes of each manufacturer are used in training step and remaining 8 OCT volumes are used for evaluation. Architecture of CNN is described in the next section.

### 3.1 CNN architecture

CNN is applied to each Bscan separately. For this task, each pixel is windowed by a [10 10] window of its neighbors. Then, these windows are input to the CNN. Therefore, each pixel is labeled as fluid or tissue by its 100 neighbors. Architecture of CNN is as follows:
First Layer: Convolution layer: number of feature maps=10, size of kernels=[3 3], activation function=rect.
Second Layer: Pooling layer: sub sample rate=2, sub sample method=mean.
Third layer: Fully-connected layer: number of nodes=150, activation function=tanh.
Fourth layer: Fully-connected layer: number of nodes=2, activation function=tanh.

The procedure to select training pixels for CNN is as follows: Consider a fluid pixel in training set, three properties including pixel intensity, average and standard deviation of the intensity of neighboring pixels are considered for this pixel. In the next step, all fluid pixels which have the properties similar to this pixel are removed from training set. Finally, a tissue pixel set with the same size of fluid pixel set is selected from tissue pixels randomly. This approach decreases the size of training set significantly since the majority of fluid pixels have the same behavior with respect to the three mentioned properties. On th other hand, ignoring such fluid pixels does not affect the performance of CNN in classification.

## 4 Segmentation results

Proposed methods for layer segmentation and layer flattening are combined with the proposed CNN architecture to segment all pixels in each Bscan as IRF, SRF, PED and tissue. Fig. 2 shows two samples of the segmented Bscans in Spectralis dataset. Also, Fig. 3 shows two samples of the segmented Bscans from Cirrus and Topcon datasets with IRF, SRF and PED. In these examples, proposed methods segment SRF, IRF and PED as shown in red, yellow and cyan colors,

respectively. Tables 1 reports the average Dice coefficients of all Bscans in test set. Proposed method achieves the average 76.44%, 92.25% and 82.14% of Dice coefficients in Cirrus, Spectralis and Topcon datasets, respectively. Note that these numbers are the average Dice coefficients in the segmentation of IRF, SRF and PED.

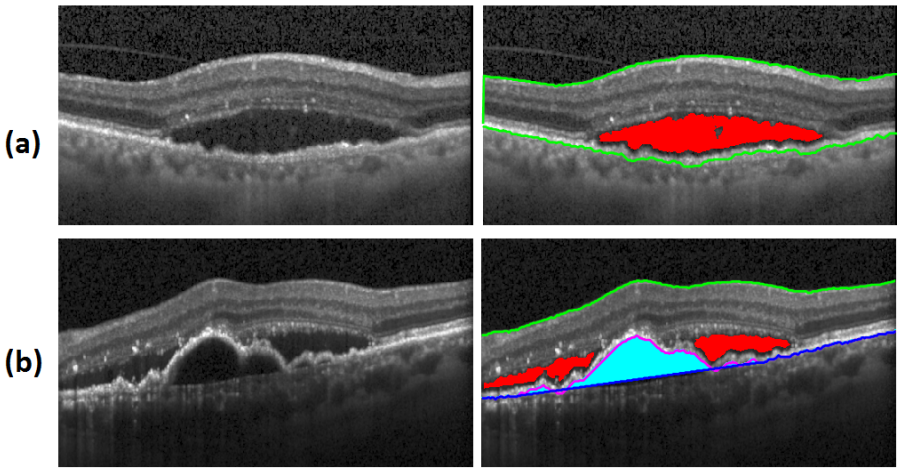


**Fig. 2.** Two samples of the segmented Bscans in Spectralis dataset. (a): SRF, (b): PED

**Table 1.** Dice Cofficient for IRF, SRF and PED segmentation in Cirrus, Spectralis and Topcon datasets.

| | Cirrus | Spectralis | Topcon |
|---|---|---|---|
| Dimension | 1024x512 | 496x512 | 885x512 |
| # of Train Bscans for IRF and SRF | 2048 | 784 | 2048 |
| # of Train Bscans for PED | 0 | 0 | 0 |
| # of Test Bscans | 1024 | 392 | 1024 |
| IRF | 78.45 | 96.24 | 81.65 |
| SRF | 69.74 | 94.53 | 79.64 |
| PED | 81.13 | 85.98 | 85.13 |
| Average | 76.44 | 92.25 | 82.14 |

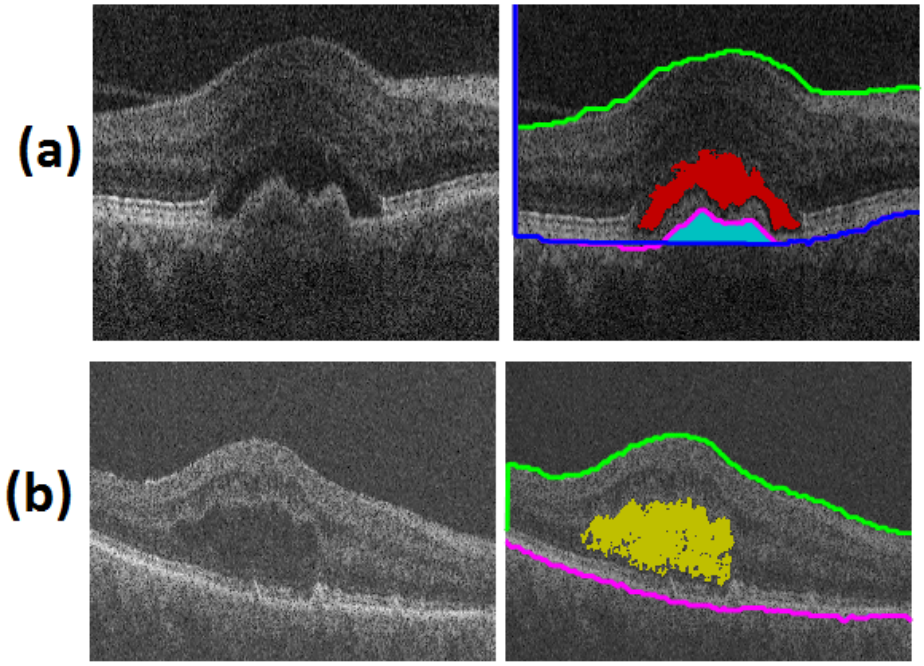


**Fig. 3.** Two samples of the segmented Bscans. (a): A Bscan from Cirrus dataset with SRF and PED, (b): A Bscan from Topcon dataset with IRF.

## 5 Conclusion

This work presented a fully-automated method to segment and detect three types of fluid including IRF, SRF and PED in OCT volumes from subjects with AMD and RVO. The proposed method is based on graph shortest path methods for layer segmentation and flattening and CNN for pixel classification. IRF and SRF are classified as fluid or tissue by CNN and an Algorithm is proposed for IRF and SRF labeling. PED is segmented by flattened RPE and elevated RPE. Results show the ability of the proposed method in the segmentation of three fluid types for different manufacturers. Future efforts will be directed towards fine-tuning the CNN to achieve better results especially in Cirrus dataset with low signal to noise ratio. Finally, reproducibility studies between segmentation following repeat imaging can be addressed as another future work.

## References

1. R. Kafieh, H. Rabbani, M. D. Abramoff, and M. Sonka, "Intra-retinal layer segmentation of 3d optical coherence tomography using coarse grained diffusion map," *Medical image analysis*, vol. 17, no. 8, pp. 907–928, 2013.
2. A. Rashno, D. D. Koozekanani, P. Drayna, B. Nazari, S. Sadri, H. Rabbani and K. K. Parhi, "Fully-Automated Segmentation of Fluid/Cyst Regions in Optical Coherence Tomography Images with Diabetic Macular Edema using Neutrosophic Sets and Graph Algorithms," *IEEE Transactions on Biomedical Engineering*, to apear, 2017.
3. J. W. Yau, S. L. Rogers, R. Kawasaki, E. L. Lamoureux, J. W. Kowalski, T. Bek, S.-J. Chen, J. M. Dekker, A. Fletcher, and J. Grauslund, "Global prevalence and major risk factors of diabetic retinopathy," *Diabetes care*, vol. 35, no. 3, pp. 556–564, 2012.
4. P. A. Keane, P. J. Patel, S. Liakopoulos, F. M. Heussen, S. R. Sadda, and A. Tufail, "Evaluation of age-related macular degeneration with optical coherence tomography," *Survey of ophthalmology*, vol. 57, no. 5, pp. 389–414, 2012.
5. K. K. Parhi, A. Rashno, B. Nazari, S. Sadri, H. Rabbani, P. Drayna, and D. D. Koozekanani, "Automated fluid/cyst segmentation: A quantitative assessment of diabetic macular edema," *Investigative Ophthalmology & Visual Science*, vol. 58, no. 8, pp. 4633–4633, 2017.
6. A. Rashno, K. K. Parhi, B. Nazari, S. Sadri, H. Rabbani, P. Drayna, and D. D. Koozekanani, "Automated intra-retinal, sub-retinal and sub-rpe cyst regions segmentation in age-related macular degeneration (amd) subjects," *Investigative Ophthalmology & Visual Science*, vol. 58, no. 8, pp. 397–397, 2017.
7. J. Kohler, A. Rashno, K. K. Parhi, P. Drayna, S. Radwan, and D. D. Koozekanani, "Correlation between initial vision and vision improvement with automatically calculated retinal cyst volume in treated dme after resolution," *Investigative Ophthalmology & Visual Science*, vol. 58, no. 8, pp. 953–953, 2017.
8. J. Wang, M. Zhang, A. D. Pechauer, L. Liu, T. S. Hwang, D. J. Wilson, D. Li, and Y. Jia, "Automated volumetric segmentation of retinal fluid on optical coherence tomography," *Biomedical Optics Express*, vol. 7, no. 4, pp. 1577–1589, 2016.
9. S. Roychowdhury, D. D. Koozekanani, S. Radwan, and K. K. Parhi, "Automated localization of cysts in diabetic macular edema using optical coherence tomography

images," in *2013 35th Annual International Conference of the IEEE Engineering in Medicine and Biology Society (EMBC)*. IEEE, 2013, pp. 1426–1429.

10. S. J. Chiu, M. J. Allingham, P. S. Mettu, S. W. Cousins, J. A. Izatt, and S. Farsiu, "Kernel regression based segmentation of optical coherence tomography images with diabetic macular edema," *Biomedical optics express*, vol. 6, no. 4, pp. 1172–1194, 2015.
11. X. Chen, M. Niemeijer, L. Zhang, K. Lee, M. D. Abràmoff, and M. Sonka, "Three-dimensional segmentation of fluid-associated abnormalities in retinal oct: probability constrained graph-search-graph-cut," *IEEE transactions on medical imaging*, vol. 31, no. 8, pp. 1521–1531, 2012.
12. G. Quellec, K. Lee, M. Dolejsi, M. K. Garvin, M. D. Abramoff, and M. Sonka, "Three-dimensional analysis of retinal layer texture: identification of fluid-filled regions in sd-oct of the macula," *IEEE transactions on medical imaging*, vol. 29, no. 6, pp. 1321–1330, 2010.